ADVANCED MATERIALS INTERFACES
Open Access
www.advmatinterfaces.de

Factors Shaping the Morphology in Sol-Gel Derived Mesoporous Zinc Titanate Films: Unveiling the Role of Precursor Competition and Concentration

*Yanan Li, Nian Li, Constantin Harder, Shanshan Yin, Yusuf Bulut, Apostolos Vagias, Peter M. Schneider, Wei Chen, Stephan V. Roth, Aliaksandr S. Bandarenka, and Peter Müller-Buschbaum**

Zinc titanate films with mesoporous structures have widespread applications ranging from sensors to supercapacitors and bio-devices owing to their photoelectric properties and specific surface area. The present work investigates the morphology of mesoporous zinc titanate films obtained by calcination of hybrid thin films containing polymer templates and precursor mixtures of zinc acetate dihydrate (ZAD) and titanium isopropoxide (TTIP). ZnO and TiO_2 films are fabricated for reference. The influences of hydrochloric acid contents (HCl), the ratios of ZAD and TTIP, and the solution concentrations on the film morphologies are studied. The amphiphilic diblock copolymer, polystyrene-*block*-polyethylene oxide (PS-*b*-PEO), plays the role of a structure directing template, as it self-assembles into micelles in a solvent-acid mixture of N, N-dimethylformamide (DMF) and HCl. Thin films are prepared with spin-coating and subsequent calcination. Adjusting the ratio of TTIP and ZAD leads to the structure evolution from order to disorder in a film. It depends on the hydrolysis and condensation processes of the precursors, providing different time-to-growth processes to control the film morphologies. An increase in solution concentration enhances the surface coverage. As probed with grazing-incidence small-angle X-ray scattering, the inner structures are larger than the surface structures seen in scanning electron microscopy.

1. Introduction

Engineered nanocrystalline metal oxide thin films with tailored mesostructures, such as titania (TiO_2) and zinc oxide (ZnO), have garnered significant attention in photovoltaics,[1] sensors,[2] and photocatalysis,[3] due to their cost-effectiveness, stability, low toxicity, and intriguing photoelectric properties. However, the performance of devices using TiO_2 and ZnO films is limited by high charge-carrier recombination rates and low electron mobility. To mitigate this issue, extensive research has been devoted to enhancing the device performance by using different surface modifications, doping strategies, and tuning property characteristics of TiO_2- or ZnO-based materials.[4] In particular, zinc titanium oxide or zinc titanate films, comprising $ZnTiO_3$ (cubic, hexagonal),[5] Zn_2TiO_4 (cubic, tetragonal),[6] and $Zn_2Ti_3O_8$ (cubic),[7]

Y. Li, N. Li, C. Harder, S. Yin, P. Müller-Buschbaum
TUM School of Natural Sciences
Department of Physics
Chair for Functional Materials
Technical University of Munich
James-Franck-Str. 1, 85748 Garching, Germany
E-mail: muellerb@ph.tum.de

N. Li
School of Physics
University of Electronic Science and Technology of China
Chengdu 610106, China

The ORCID identification number(s) for the author(s) of this article can be found under https://doi.org/10.1002/admi.202400215

DOI: 10.1002/admi.202400215

C. Harder, Y. Bulut, S. V. Roth
Deutsches Elektronen-Synchrotron DESY
Notkestrasse 85, 22607 Hamburg, Germany

S. Yin
School of Mathematics and Physics Jiangsu University of Technology
Changzhou 213001, China

A. Vagias
Institut Laue-Langevin
6 rue Jules Horowitz, Grenoble 38000, France

P. M. Schneider, A. S. Bandarenka
TUM School of Natural Sciences Department of Physics Physics of Energy Conversion and Storage
Technical University of Munich
James-Franck-Str. 1, 85748 Garching, Germany

W. Chen
Shenzhen Key Laboratory of Ultraintense Laser and Advanced Material Technology, Center for Intense Laser Application Technology, and College of Engineering Physics
Shenzhen Technology University
Shenzhen 518118, China

have demonstrated advantages such as the low charge carrier recombination rate,[8] optimized bandgap and enhanced electron mobility.[9] As well-known from metal oxides, the film morphology also plays a critical role on the achievable device performance.[10] In particular, compared to conventional nanoparticle-based films, which are challenged by agglomeration issues, mesoporous films with interconnected network architectures are beneficial for efficient charge transport, improved stability, and increased surface-to-volume ratio providing an enhanced active-site density for surface reactions.[11] For example, Chi et al. prepared mesoporous $ZnTiO_3$ rods with good photocatalytic activity and low costs, which could offer broad opportunities for environmental remediation.[12] However, in contrast to TiO_2 and ZnO films, tailoring series of zinc titanate film morphologies are rarely reported in the literature,[8,13] especially rarely reported are the factors related to solute and solvent. Hence, studying mesoporous morphologies of zinc titanate films with a controlled domain configuration is highly meaningful and necessary, to enable new chances for device performance improvements in the future.

At present, compared to physical vapor deposition, chemical vapor deposition (CVD), micro-arc oxidation, and thermal spray processes,[14] thin film fabrication routes based on sol-gel chemistry in combination with spin-coating appear attractive to achieve a controlled thin film structure in laboratory conditions due to its ease in tailoring the process. In the sol-gel chemistry route, block copolymers (BCPs), such as polystyrene-*block*-polyethylene oxide (PS-*b*-PEO), are very successfully used to template the resulting mesoporous metal oxide films via the control of the self-assembled micellar structures loaded with the precursors.[15] The controlling factors of the BCP template morphologies (tubules, vesicles, rods, and lamellae) are molecular weight, solvent evaporation,[16] salt content,[17] concentration,[18] temperature,[19] *etc.* In the complex film formation process, contributions from the free surface energy, interfacial energies including the interactions with two blocks of the BCP, elastic energies including chain conformations, and interaction energies with the substrate drive the film morphology.[20] Usually, ion addition for controlling the template morphologies has been used to impart functionality or affect the interfacial energetics.[21] The formed hybrid micellar structures are densely packed in the solid phase, and the precursor molecules bonding with the polymer blocks affect the interfacial energy during the film formation.[22] Desired film morphologies were achieved, e.g., by controlling the solvent and additive contents,[23] by optimizing the annealing temperature and time,[24] by utilizing the polymer or nanoparticle templates.[25] Jiang et al. prepared TiO_2 films with ordered structures by adjusting the solvent composition and the hydrolysis rate of $TiCl_4$.[26] Tian et al. prepared mesoporous ZnO films with worm-like, sponge-like, and grid-like structures using zinc acetate dihydrate (ZAD) and PS-*b*-PEO with different molecular weights and PS-*b*-P4VP, respectively, having an almost positive relationship between adsorption and electrical conductivity.[27]

However, the existing studies on zinc titanate composite thin films are still inadequate, especially using the precursor mixture of the highly reactive titanium isopropoxide (TTIP) and ZAD with less hygroscopicity and no oxidizing properties. For example, Sarkar et al. fabricated foam-like zinc titanate films with large aggregates based on the BCP-assisted sol-gel chemistry using ZAD and ethylene glycol-modified titanate (EGMT) by spray-coating, an industry-oriented approach, at 80 °C. Zinc orthotitanate films were obtained by calcination at 600 °C.[28] They used solutions containing PS-*b*-PEO (23 kg mol^{-1} for PS block; 7 kg mol^{-1} for PEO block), ZAD and EGMT dissolved in a mixture of N, N-dimethylformamide (DMF), water, and hydrochloric acid (HCl). However, the obtained film surfaces exhibited large aggregates without ordered structures. Also the role of HCl in the system was not discussed in the earlier work. Ehsan et al. prepared globular zinc titanate-titania particles using TTIP and ZAD by aerosol-assisted CVD.[29] Chuaicham et al. showed the high photocatalytic phenol degradation performance of the $ZnTiO_3$ phase, which was prepared based on the precursor mixture of zinc nitrate hexahydrate and titanium chloride, using the hydrothermal synthesis method.[8] However, to the best of our knowledge, so far there is no systematic study on the factors of the BCP template, the crystal type when changing the ratio of TTIP and ZAD, and acid function based on the competitive relationship between TTIP and ZAD during their hydrolysis process.

Herein, we investigate the morphology of the hybrid films prepared with a PS-*b*-PEO template and a mixture of two precursors before calcination as well as the morphology of the resulting zinc titanate films after calcination. The film morphologies are adjusted by changing the composition (precursor ratio of TTIP and ZAD), solution concentration, and hydrochloric acid (HCl) content in the stock sol-gel solution preparation. As additives, the precursors and the acid affect the interfacial energy between the blocks of the BCP causing a polymer-structure reorganization, which can be used to tune the film morphology. For reference, the metal oxide films TiO_2 or ZnO are fabricated as well when using the pure precursors TTIP or ZAD. Due to the different hydrolysis reactions of TTIP and ZAD, the additional HCl will not only decelerate the hydrolysis rates of TTIP and ZAD but also prevent aggregation formation in the solution.[30] In addition, the growth of anatase TiO_2 with small grains is driven by the strong bonding of HCl on the TiO_2 (101) surface, Cl^- is a rutile mineralizer, and a high HCl concentration is beneficial for the formation of smaller-scale building blocks.[31] Moreover, due to the presence of additional ions, the surface morphology of a film can be different from the inner film structure.[32] In this work, the fabricated film morphologies are probed with scanning electron microscopy (SEM) to picture the surface morphologies and with grazing-incidence small-angle X-ray scattering (GISAXS) to study the inner structure. The crystal phases of the calcined films are characterized with grazing-incidence X-ray diffraction (GIXD).

S. V. Roth
Department of Fibre and Polymer Technology
KTH Royal Institute of Technology
Teknikringen 56–58, Stockholm SE-100 44, Sweden

A. S. Bandarenka
Catalysis Research Center
Technical University of Munich
Ernst-Otto-Fischer-Straße 1, 85748 Garching, Germany

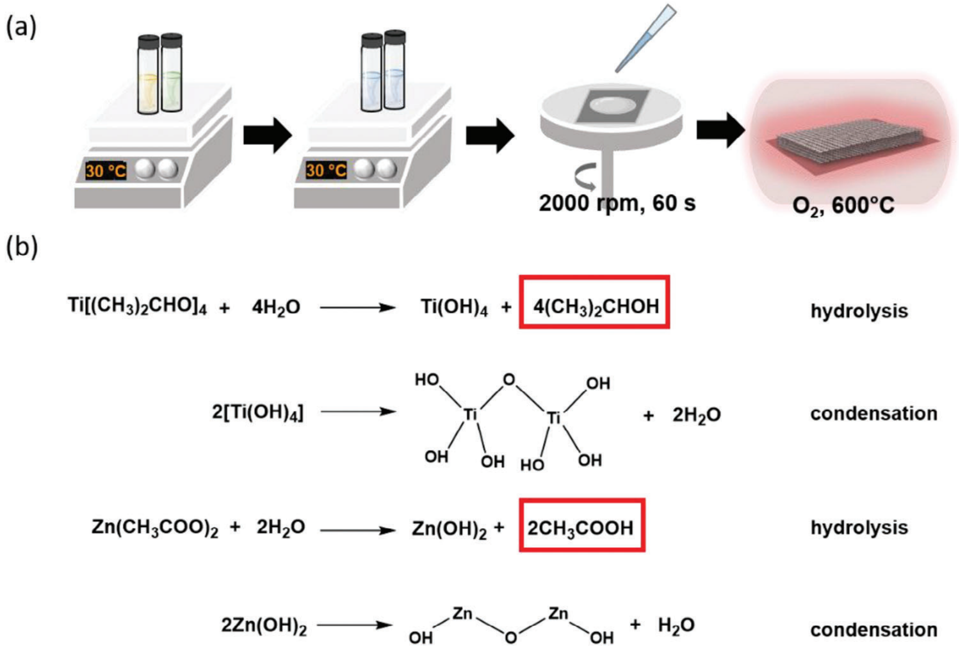

Figure 1. a) Schematic illustration of the fabrication of mesoporous thin zinc titanate films. Initially, the PS-*b*-PEO solutions with TTIP or ZAD are prepared separately in two vials. After that, the solutions are intermixed to obtain the solutions with polymers and the two precursor mixtures. Then, the solutions are spin-coated on pre-cleaned Si substrates. After two days, the thin films are calcined at 600 °C to remove the polymer templates. b) Illustration of hydrolysis and condensation reactions of TTIP and ZAD for zinc titanate production.

2. Results and Discussion

The mesoporous zinc titanate films with various morphologies are fabricated via calcining the spin coated hybrid films (**Figure 1**). For reference, the metal oxide films TiO_2 or ZnO are fabricated as well. In this work, we compared two series samples, which differ in the HCl content: Series A and series B have a low and a high HCl content, respectively. In series A, the mass ratio of PS-*b*-PEO, HCl, and precursors in solution is fixed at $m_{PS\text{-}b\text{-}PEO}:m_{HCl}:m_{precursors}$ = 1:2:2. In series B, these three reactants are fixed at $m_{PS\text{-}b\text{-}PEO}:m_{HCl}:m_{precursors}$ = 1:4:2. Based on the solubility parameters of polymers and solvents (Table S1, Supporting Information), the self-assembled micellar structure of PS-*b*-PEO has a PS core and a PEO shell in a solution. The presence of DMF, which is a suitable solvent for both blocks, and HCl, which can protonate the PEO block, probably result in the formation of spherical micelles due to the balanced solubility of both blocks in the solvent mixture. Moreover, the block copolymer length and packing parameter influence a micellar size and shape, suggesting variations under different conditions. Following the loading of precursors binding with PEO blocks due to hydrogen bonds, the micellar structure transits from a sphere to a cylinder. This conclusion is supported by Tian et al., who observed that the loading of ZAD caused spherical micelles to change to cylindrical structures with core and shell sizes of 9 nm and 1.8 nm, respectively.[33]

For both series (A and B) we investigate three different solution concentrations labeled as dilute (c1), intermediate (c2), and concentrated (c3) solution groups. In each solution group, four different mass ratios of the precursors TTIP to ZAD (10:0, 5:5, 3:7, and 0:10) are prepared. Accordingly, depending on the precursor ratio, we obtain the zinc titanate composite films as well as TiO_2 or ZnO reference films. The hybrid thin films composed of polymers and precursors are obtained by spin-coating these different solutions on silicon substrates pre-cleaned in an acid bath.[34] The accordingly prepared 24 samples of the series A and B are summarized in Table S2 (Supporting Information). To obtain the zinc titanate films and reference samples, the hybrid films are calcined at 600 °C in the air as described in the experimental section.

We use thermogravimetric analysis (TGA) to investigate the thermal stability of PS-*b*-PEO and further to prove that the polymer template is completely removed under the above thermal-treatment condition. Figure S1a (Supporting Information) shows two peaks, which means that PEO and PS are decomposed at 347 °C and at 448 °C, respectively. The TGA condition setting is the same as the calcination process of the hybrid films (Figure S1b, Supporting Information). Therefore, the polymer template is totally combusted once the temperature reaches 486 °C. During the calcination step, besides the polymer template removal from the hybrid film, the thermal treatment enables the remaining amorphous titania and zinc to crystallize.

2.1. Film Morphology

2.1.1. Hybrid Films Prepared with Low HCl Content

SEM surface images of the 12 hybrid films combining polymers and precursors from the A series are shown in **Figure 2** before calcination. The three different concentrations are shown from left to right for dilute (c1, Figure 2a–d), intermediate (c2,

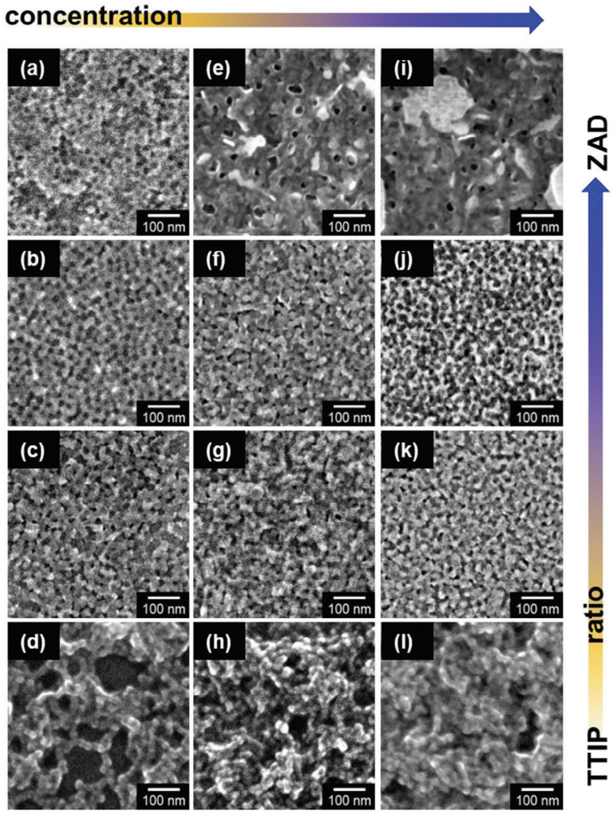

Figure 2. SEM images of hybrid thin films in series A before calcination. The ratios of the two precursors m_{TTIP}:m_{ZAD} are 10:0, 5:5, 3:7, and 0:10 (from the bottom to the top row). The material mass of the film (prepared using dilute, intermediate, and concentrated solutions) increases from the left to the right column.

Figure 2e–h), and concentrated (c3, Figure 2i–l) samples, respectively. The four different precursor ratios (TTIP: ZAD = 0:10, 3:7, 5:5, and 10:0) are shown from the top to bottom in Figure 2. For the dilute solution and with an increase of the ZAD addition, the film morphologies transform from a more inhomogeneous surface with disordered structures into a more uniform surface with better-ordered structures, e.g., forming a porous film with a well-defined pore size (≈20 nm) (Figure 2b). Compared with TTIP, ZAD undergoes hydrolysis more readily due to its chemical structure. The differing sensitivities of isopropyl alcohol and acetic acid to HCl mean that additional HCl prevents the formation of aggregates. Thus, increasing the ZAD content in the precursor mixture helps in a delayed aggregate formation, facilitating the maintenance of the polymer template. Notably, this is beneficial for the formation of elongated more ordered structures instead of forming compact aggregates since the encapsulation of the PEO shell domains by hydrolysis products of the precursors alters the block interactions between PEO and PS. With an increase in material mass, the morphologies become more compact due to more precursor material present in the solution. In case of pure ZAD (Figure 2a,e,i), the film transforms from a better-ordered morphology into more disordered structures having fewer and large pores when increasing the concentration. In case of pure TTIP (Figure 2d,h,l), the aggregated films with network structures become more compact when increasing the concentration. In case of TTIP and ZAD mixtures (Figure 2b,f,j), the films show rather uniform surfaces with ordered structures irrespective of the concentration. For the TTIP to ZAD ratio of 3 to 7, the characteristic surface structure size is approximately 20 nm, as depicted in Figure 2b,f,j. This observation can be attributed to the influence of ZAD on the hydrolysis rate of TTIP, contributing to a decrease in large aggregates and promoting their uniform dispersion around polymer templates. Changing the material concentrations (Figure 2c,g,k) affects the porosity but not the film uniformity. Overall, the films (Figure 2c,g,k) at the ratio of 5:5 (TTIP: ZAD) show similar behavior as observed in the composite films (Figure 2b,f,j).

To investigate the inner structures of the hybrid thin films, we perform GISAXS measurements. The two-dimensional (2D) GISAXS data are shown in Figure S2 (Supporting Information). At the ratio of 3:7 (TTIP: ZAD) (Figure S2b, f, j, Supporting Information), the 2D GISAXS data exhibit clear Bragg rods, indicating the existence of ordered structures with a well-defined distance. With increasing concentration at a fixed precursor ratio, the Bragg rods remain unchanged, which confirms that the characteristic structures do not depend on the material concentrations in agreement with the SEM observations. To extract more detailed in-plane structural information from the GISAXS data, we perform horizontal line cuts at the Yoneda peak position and model these line cuts. The details about the GISAXS modeling are provided in the Supporting Information. Three characteristic-cylindrically shaped objects are needed to explain the scattering data.[35] The three cylindrical objects have the same height but different radii and center-to-center distances (d_{cc}), which describe the dispersing state of the objects. Concerning the "small" size domains, in the hybrid thin film, the polymer or precursors can form small aggregates. Thus, the small domains can be polymer coils or polycondensation products of the precursors. The "medium" size domains describe the micellar structures loading precursors. Concerning the "large" size domains, before calcination, due to solvent evaporation, primary micelles have the trend to combine. After calcination, collapsed structures can form large structures. The horizontal line cuts are present in **Figure 3**a–c and the extracted values for the object radii and their corresponding center-to-center distances are presented in Figure 3d–f and Figure S3a–c (Supporting Information), respectively. The scattering curves show pronounced differences indicative of the different order degrees as seen in SEM.

The three cylinder-object radii (s, m, and l) of a film are distributed at 3.0 – 7.3, 7.3 – 16.3, and 36.0 – 53.0 nm (Figure 3d–f), respectively. The related center-to-center distances (d_{cc}) between two neighboring objects ranges from 23.0 ± 3.0 to 330.0 ± 30.0 nm. In the case of the dilute solution-based films (Figure 3d), with increasing ZAD content, the large-object radii are in the range of 40.0 – 53.0 nm and the d_{cc} values increase from 100.0 ± 10.0 to 330.0 ± 30.0 nm. The small- (5.8 ± 0.3, 5.1 ± 0.2, 5.5 ± 0.5, 7.0 ± 0.3 nm) and middle-object radii (10.0 ± 0.5, 10.5 ± 0.5, 11.0 ± 0.5, 16.0 ± 0.3 nm) increase as well. The corresponding d_{cc} values are (23.0 ± 3.0, 33.0 ± 5.0, 26.0 ± 1.0, 35.0 ± 10.0 nm) and (45.0±5.0, 40.0±10.0, 45.0±20.0, 60.0±20.0 nm), respectively. In general, the small-, middle- and large-object radii of the intermediate and concentrated samples (Figure 3e,f) show similar values as the counterparts of the diluted (Figure 3d).

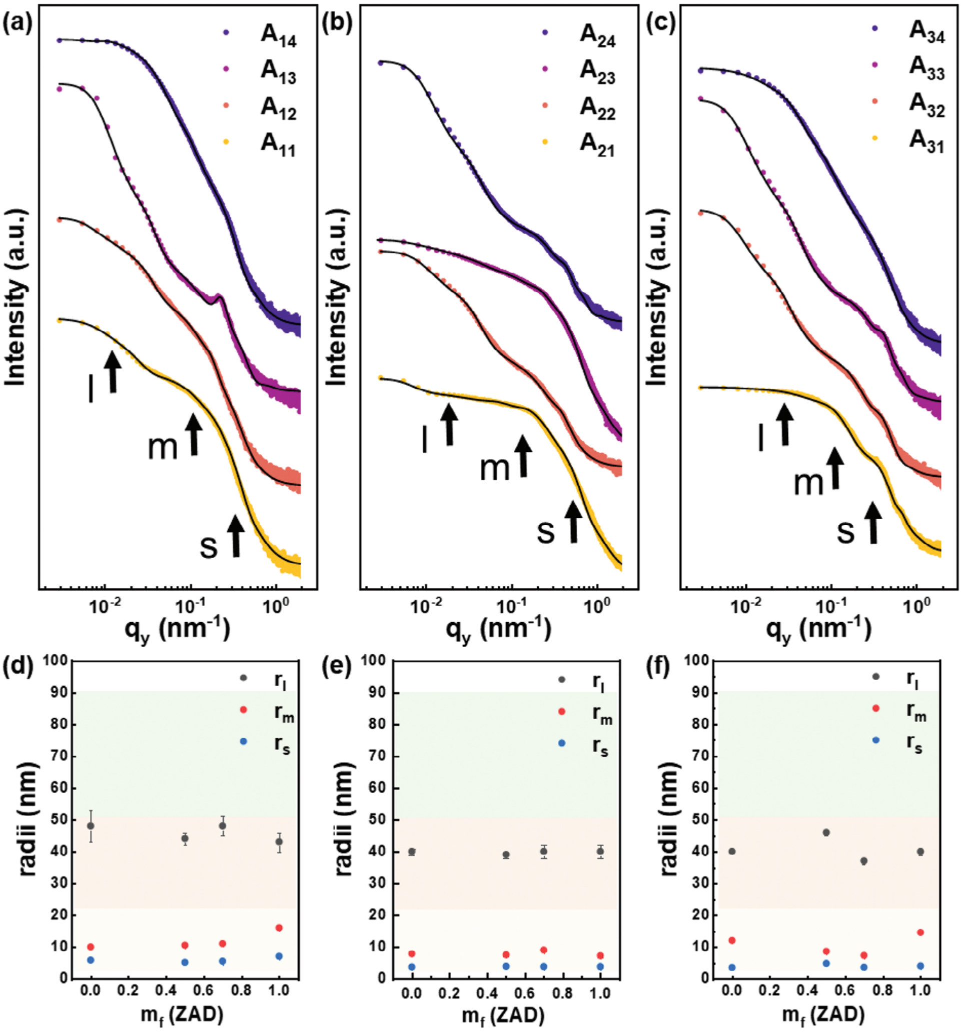

Figure 3. a–c) Horizontal line cuts from 2D GISAXS data of hybrid thin films in series A before calcination. The measured data are represented as solid circles and the modeling results are depicted as solid lines. To improve clarity, all curves have been shifted along the intensity axis. For the films using (a) dilute, (b) intermediate, and (c) concentrated solutions, the ratios of m_{TTIP}:m_{ZAD} is 10:0, 5:5, 3:7, and 0:10 from bottom to top, respectively. Contributions from small (s), middle (m) and large (l) objects are indicated with the arrows. d–f) Extracted characteristic structure radii as a function of the mass ratio of ZAD in a precursor mixture, m_f (ZAD) for the films using (d) dilute, (e) intermediate and (f) concentrated solutions. With different colors the small (blue, r_s), middle (red, r_m), and large (black, r_l) objects are shown.

However, at high concentrations, the radii of the middle objects decrease due to the formation of more compact structures, particularly in concentrated solution-based films (Figure 3f). Compared with the films based on dilute solutions, the domain sizes in films based on intermediate and concentrated solutions are smaller for both small- and middle-sized domains, especially in films containing precursor mixtures. Nevertheless, films based on concentrated solutions containing either TTIP or ZAD exhibit larger domain sizes than those based on intermediate solutions. This issue might be addressed by increasing the HCl content to better isolate the micelles. These results are consistent with the SEM observations. Thus, the introduction of ZAD hinders the condensation of TTIP to avoid aggregate formation. The more random d_{cc} values in films with pure TTIP or ZAD is attributed to aggregation. With increasing material mass these d_{cc} values of the films with precursor mixtures decrease for the small and middle cylindrical domains (Figure S3, Supporting Information), meaning that the object distances decrease and the film area increases.

Besides object radii and distances, the quantity of objects present in the hybrid films is extracted from the GISAXS data analysis (Figure S6d–f, Supporting Information).[36] For comparison, the SEM images are statistically analyzed using Image J (Figure S6a–c, Supporting Information). In this presentation in Figure S6 (Supporting Information), we stick to the three cylindrical objects small, middle and large as shown in yellow, red and green bars, respectively. At the surface of the hybrid films, we see a dominance of small objects (yellow), while for the inner structures the middle objects (red) are dominating in Figure S6 (Supporting Information). Accordingly, the inner structure object radii are predominantly larger than the surface, which is probably due to a solvent evaporation gradient from the film-air

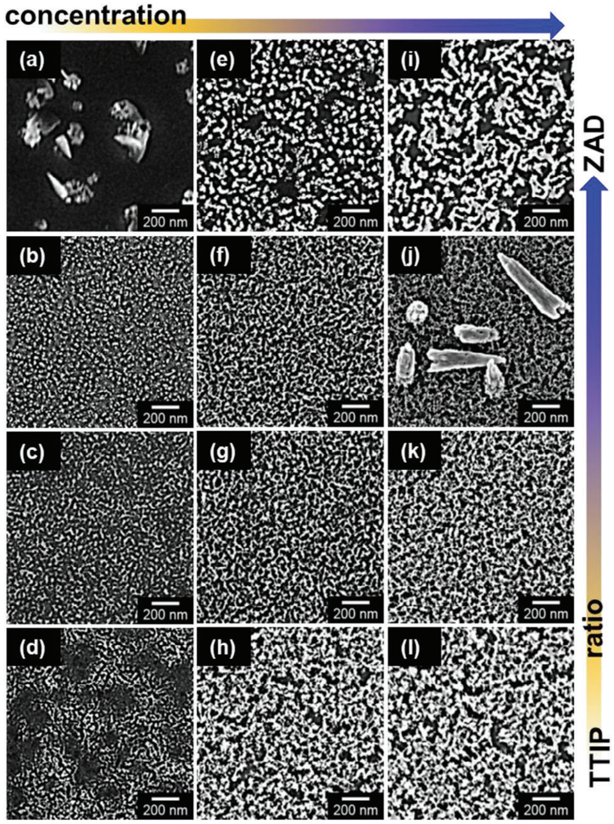

Figure 4. SEM images of zinc titanate and reference oxide thin films in series A after calcination. The ratios of the two precursors m_{TTIP}:m_{ZAD} are 10:0, 5:5, 3:7, and 0:10 (from the bottom to the top row). The material mass of the film (prepared using dilute, intermediate, and concentrated solutions) increases from the left to the right column.

interface to the film-substrate interface. This notion is supported by the findings of Rejek et al., who observed a lamellae surface and cylindrical inner structures of a solution-based film containing PS-*b*-PEO and TiO_2 nanoparticles.[32b]

2.1.2. Zinc Titanate Films Prepared with Low HCl Content

Via calcination, the hybrid films are transformed into the zinc titanate films and into oxide films for the reference samples (**Figure 4**). The calcined thin films prepared from dilute solutions do not fully cover the substrate (Figure 4a–d). In particular, the reference ZnO film exhibits large bare substrate areas due to the removal of the large polymer aggregates formed during the preparation (Figure 4a). In contrast, the zinc titanate films are uniformly covering the surface with small objects (Figure 4b,c,f,g) due to the initially uniform polymer template coverage. To achieve a better coverage of the thin films on the substrates, higher concentrations are used successfully. With increasing material mass of the film from the left column to the right column (Figure 4), the bare areas decrease in the TiO_2 or ZnO films. The zinc titanate films show uniform film surfaces and condensed structures with increasing material mass when (m_{TTIP}:m_{ZAD} = 5:5), while with concentration increase, the films (m_{TTIP}:m_{ZAD} = 3:7) show two-layer structures consisting of a condensed small structure layer and a layer with rod-like nanoparticles (200–600 nm) (Figure 4j). The overall surface morphology of the film (Figure 4j) is shown in Figure S4 (Supporting Information). Compared to the single-layer porous structures, the two-layer structures offer the advantage of having additional nanoparticle-based structures with interconnected channels,[11] extending their potential optoelectronic applications.

Compared to the TiO_2 and ZnO films, generally, the zinc titanate films have smaller domain sizes on the film surfaces (Figure 4). Since the calcination process may collapse the formed structures inside the films. Again, GISAXS measurements were performed to obtain statistically significant morphology information and the 2D GISAXS data of the calcined films are shown in Figure S5 (Supporting Information). Figure S5b (Supporting Information) clearly shows the typical Bragg rods indicating the presence of ordered structures within this film when m_{TTIP}:m_{ZAD} = 3:7. With increasing material mass, the Bragg rods become blurred due to a wide structure distribution in thicker films. The horizontal line cuts of the 2D GISAXS data are shown in **Figure 5**. For a detailed analysis, these line cuts are modeled with the same model as used for the hybrid films. Figure 5d–f and Figure S6a–c (Supporting Information) display these modeling results. The large cylindrical object radii of the zinc titanate films (Figure 5d,e) are smaller than that of the bare TiO_2 and ZnO films, in agreement with the SEM results seen in Figure 4. For the dilute solution-based films (Figure 5d), the middle-object radii increase from 8.0 ± 0.5 nm to 12 ± 0.3 nm with increasing the ZAD content, the small domains are unchanged in the 3.1 – 4.1 nm range. For the dilute solution-based films (Figure 5e), we can observe the same trend for the large, middle, and small objects having a radii range of 3.3 – 4.2 nm. However, for the concentrated solution-based films (Figure 5f), with increasing the ZAD content, large-object radii (from 13.5 ± 0.5 nm to 47.0 ± 0.3 nm) increase, and middle and small domains unchanged (8.3 – 8.7 nm and 3.5 – 3.8 nm). Overall, the d_{cc} values of the large object in the TiO_2 or ZnO films are larger than that of zinc titanate films (Figure S6, Supporting Information) due to the formed aggregates with a disordered distribution within the films since the added ZAD may break the networking of TTIP to form small structures. With increasing material mass in the film, the d_{cc} values of three different object types decrease (Figure S6, Supporting Information) indicating that the structures are packed and condensed to form a dense film. Therefore, the calcined films are denser when increasing the concentration, and using the precursor mixture can prevent the formation of large aggregates at a certain degree during the calcination process.

Again, the quantity of domains present in the calcined films is extracted from the GISAXS data analysis (Figure S7j–l, Supporting Information)[36] and compared with the SEM results (Figure S7g–i, Supporting Information). Changes are seen between the inner and surface structures for the three used classes of objects in the modeling (small, middle, and large). Compared to the surface morphologies (Figure S7g–i, Supporting Information), which are dominated by small domains, the inner structures of the films (Figure S7j–l, Supporting Information) mainly contain middle-sized objects. With increasing material mass, the middle-sized domains also appear on the film surface. The inner structure of the calcined films (Figure S7j, k, Supporting

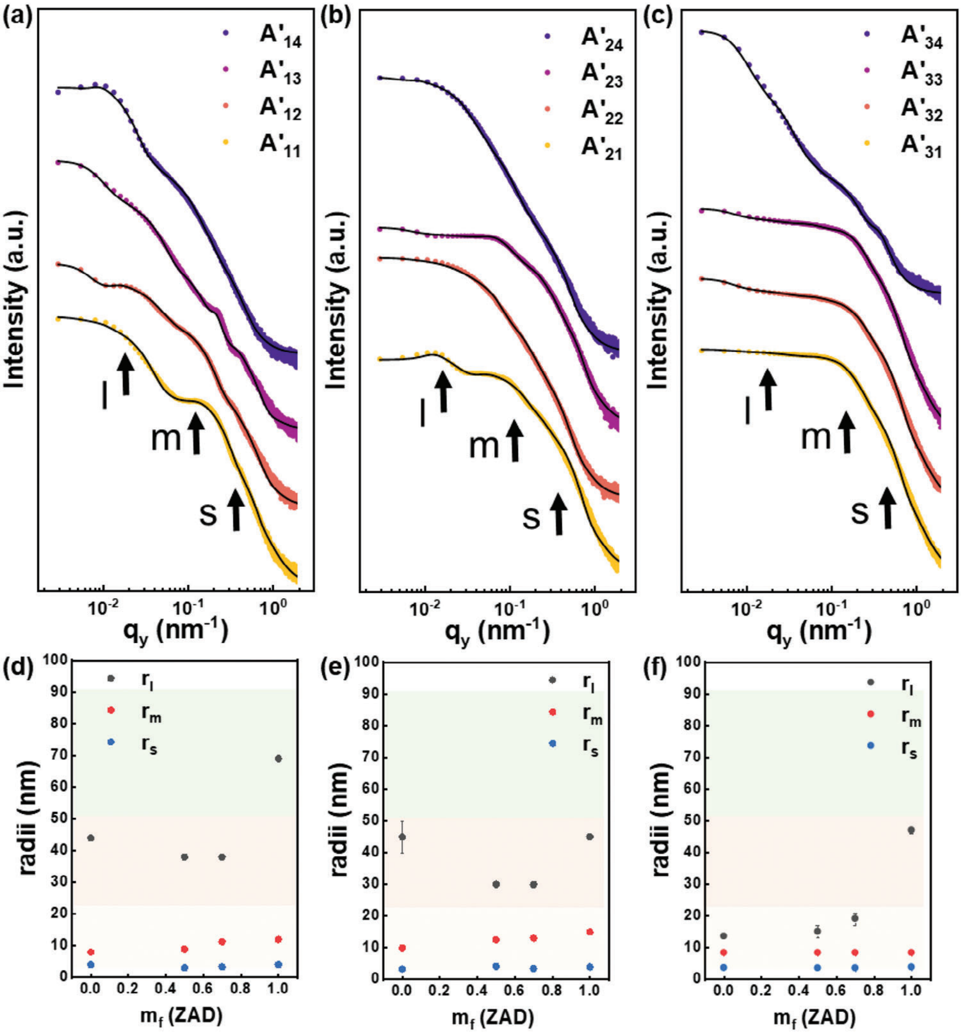

Figure 5. a–c) Horizontal line cuts from 2D GISAXS data of zinc titanate and reference oxide thin films in series A after calcination. The measured data are represented as solid circles and the modeling results are depicted as solid lines. To improve clarity, all curves have been shifted along the intensity axis. For the films using (a) dilute, (b) intermediate, and (c) concentrated solutions, the ratios of m_{TTIP}:m_{ZAD} are 10:0, 5:5, 3:7, and 0:10 from bottom to top, respectively. Contributions from small (s), middle (m), and large (l) objects are indicated with the arrows. d–f) Extracted characteristic structure radii as a function of the mass ratio of ZAD in a precursor mixture, m_f (ZAD) for the films using (d) dilute, (e) intermediate, and (f) concentrated solutions. With different colors the small (blue, r_s), middle (red, r_m), and large (black, r_l) objects are shown.

Information) is dominated by larger objects for the ZnO film. These results are well consistent with the above discussion.

2.1.3. Hybrid Films Prepared with High HCl Content

In series B with high HCl content, the precursor condensation delays so the material mass and precursor ratio effect will differ. Again, before calcination, due to the presence of the PS-*b*-PEO template, we obtain hybrid films. The variation ratios of m_{TTIP}:m_{ZAD} are the same as in series A 10:0, 5:5, 3:7, and 0:10. When comparing the SEM images of series B (**Figure 6**), the influence of the concentration and precursor ratio is not as pronounced as in the series A. Thus, when increasing the HCl content, the hybrid film preparation becomes more robust against changing these parameters. The pure ZnO films exhibit the best-ordered morphologies in series B (Figure 6a,e,i), whereas the pure TiO_2 films have perhaps the worst-ordered morphologies (Figure 6d,h,l). With mixed precursors, rather closely packed globular structures are seen. Figure S7 (Supporting Information) presents the respective 2D GISAXS data of the calcined films. The presence of Bragg rods in the 2D GISAXS data, indicative of ordered and periodic structures within the films, aligns with the ordered surface morphologies depicted in Figure 6a,e,i. Notably, as the ZAD contents within the films increase, a transition from disorder to order in the structural arrangement becomes evident. Moreover, it is observed in Figure S8b, f, j (Supporting Information) that the Bragg rods become less distinct with increasing concentration.

We perform horizontal line cuts in the 2D GISAXS data at the Yoneda peak position for further analysis. In **Figure 7a–c** these line cuts are shown alongside their corresponding model fits and

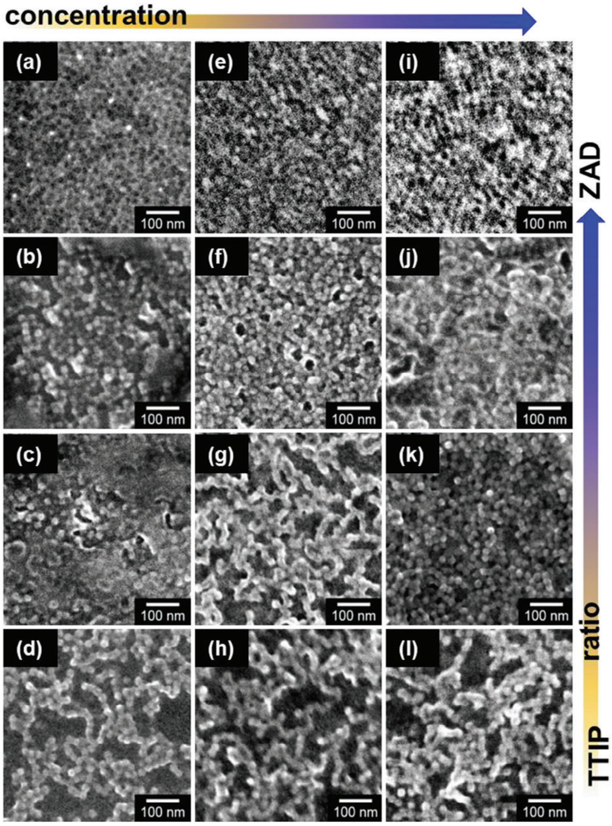

Figure 6. SEM images of hybrid thin films in series B before calcination. The ratios of the two precursors m_{TTIP}:m_{ZAD} are 10:0, 5:5, 3:7, and 0:10 (from the bottom to the top row). The material mass of the film (prepared using dilute, intermediate, and concentrated solutions) increases from the left to the right column.

Figure 7d–f depicts the object sizes extracted from the model results. Compared to the dilute solution-based films, the intermediate and concentrated solution-based films have smaller object radii than the dilute solution-based films. Notably, in the dilute solution-based films, which are characterized by the presence of large aggregates, the object-size variations do not follow a consistent pattern with increasing ZAD content (Figure 7d). In contrast, for the intermediate and concentrated solution-based films the increase in the ZAD content causes an increase in the size of all the large, middle, and small objects (Figure 7e,f). When looking to the d_{cc} values (Figure S9, Supporting Information), it is found that an increase in concentration within the film leads to the formation of a denser stacking of self-assembled structures consisting of PS core and PEO shell with precursors. Overall, for the intermediate and concentrated solution-based films, the distances between these objects (large, medium, small) show a similar tendency as in the counterpart of the object size with the introduction of additional ZAD content within the film. Therefore, with increasing concentration, we fabricate more dense films on the substrate and the object sizes decrease due to the compact structures. As the quantity of ZAD increases, the object size consistently increases due to polymer aggregation caused by a decreasing quantity of ions. ZAD displays greater sensitivity to HCl than TTIP, resulting in an aggregate formation delay.

When looking to the quantity of domains present in the hybrid films of series B (Figure S13a–f, Supporting Information), the surface morphologies of the films before calcination are dominated by the small-sized objects (Figure S13a–c, Supporting Information), whereas the inner structures again tend to be larger and predominantly are formed by middle-sized objects (Figure S13d–f, Supporting Information). In the case of dilute and intermediate solution-based films (Figure S13d, e, Supporting Information), the precursor ratios do not significantly affect the volume fractions of objects. However, at high concentrations, the volume fraction of small-sized objects becomes dominant.

Compared to the films of series A, in which precursor ratio and concentration do not offer obvious trends on the film morphology evolutions, the films of series B with high HCl content show relatively clear trends. In series B, with increasing ZAD content, the object sizes increase for the intermediate solution and concentrated solution-based films; with increasing concentration, the domain sizes decrease, and the quantity of small domains increases. In addition, the increasing HCl content increases the quantity of small domain sizes since more ions surround polymer structures hindering aggregation. Thus, increasing the HCl content is beneficial for systematically controlling the domain sizes and observing the effects of precursor ratio and material mass on the film morphologies.

2.1.4. Zinc Titanate Films Prepared with High HCl Content

Figure 8 illustrates the surface morphologies of the corresponding films presented in Figure 6, after the calcination process. Different from series A, some samples undergo strong morphology changes due to a high temperature-induced pattern collapse. In the case of pure ZAD, the obtained ZnO films (Figure 8a,e,i) show sheet-like or rod-like structures dispersed across the substrate instead of the initially ordered nanostructure. With increasing TTIP content, the initial mesoporous nanostructure is better preserved as seen in the pure TiO_2 films (Figure 8d,h,l). The two-layer structure films (Figure 8b,f,j) are formed in series B, which is similar to the film structure (Figure 4j). The cross-section image of the dilute-solution based film (Figure 8b) is shown in Figure S10 (Supporting Information). In the case of the zinc titanate films, the resilience of the mesoporous nanostructure improves with concentration and TTIP content. Notably, the various resulting structures not only rely on the template but also emphasize the significance of the calcination process, which may alter the morphology through a structure collapse and crystallite formation.

2D GISAXS data (Figure S11, Supporting Information) provide information about the inner film structures. The presence of discernible Bragg rods in Figure S11b, f, j (Supporting Information) signifies the existence of well-ordered structures within these films. Conversely, a broad dispersion of domains is present in patterns without such clear Bragg rods. To further corroborate this observation, we conduct horizontal line cuts at the Yoneda peak position and model them as explained (**Figure** 9a–c). The corresponding radii and d_{cc} results are presented in Figure 9d–f and Figure S12a–c (Supporting Information). Notably, the small- and middle-object radii are almost content, covering a range of 3.4 – 4.5 nm and of 8.5 – 15.0 nm with increasing ZAD content.

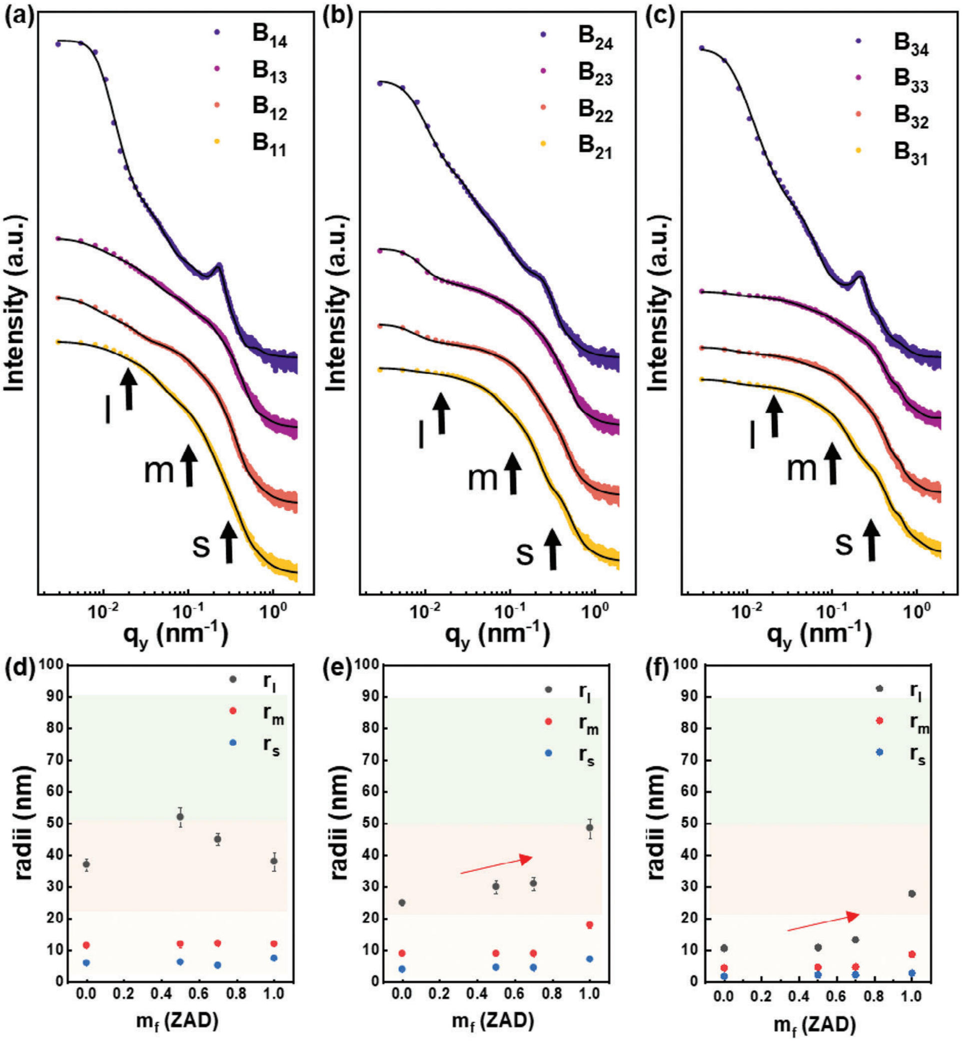

Figure 7. a–c) Horizontal line cuts from 2D GISAXS data of hybrid thin films in series B before calcination. The measured data are represented as solid circles and the modeling results are depicted as solid lines. To improve clarity, all curves have been shifted along the intensity axis. For the films prepared using (a) dilute, (b) intermediate, and (c) concentrated solutions the ratios of m_{TTIP}:m_{ZAD} is 10:0, 5:5, 3:7, and 0:10 from bottom to top, respectively. Contributions from small (s), middle (m), and large (l) objects are indicated with the arrows. d–f) Extracted characteristic structure radii as a function of the mass ratio of ZAD in a precursor mixture, m_f (ZAD) for the films using (d) dilute, (e) intermediate, and (f) concentrated solutions. With different colors the small (blue, r_s), middle (red, r_m), and large (black, r_l) objects are shown.

In contrast, the large-object radii in the calcined films increase in response to an increasing ZAD content, to very large values, which is caused by the pattern collapse and crystallite formation (Figure 8). Accordingly, the structures are larger in series B than those in series A. In Figure S12a (Supporting Information), it becomes apparent that also the center-to-center distances between large domain sizes increase in response to an increase in the ZAD content. No clear trends are seen in the cross-over from pattern collapse to the preservation of the templated morphology for the small and middle-size objects.

When evaluating the volume fractions of the calcined films (Figure S13g–l, Supporting Information) only a few trends from series A are seen as well. For the calcined films, in the case of the surface morphologies as seen by SEM, the small domain sizes continue to dominate the film surface. Regarding the inner structures of the films, an increase in material mass leads to a significant reduction in domain sizes within films (m_{TTIP}:m_{ZAD} = 10:0 and 5:5). In contrast, films with m_{TTIP}:m_{ZAD} ratios of 3:7 or 0:10 exhibit stable domain sizes predominantly in the middle range. Therefore, ZAD content displays an important role in the object size growth and the film density increase.

2.2. Crystal Structure

Besides the film morphology, its crystal structure is also of importance. Here, we restrict to the calcined films as the hybrid films are amorphous. **Figure 10** shows the GIXD results for the films prepared with different ratios of TTIP and ZAD using a low and high HCl content together with a high solution concentration. Characteristic Bragg peaks are marked. Irrespective of the HCl content, for pure ZAD as expected zincite ZnO

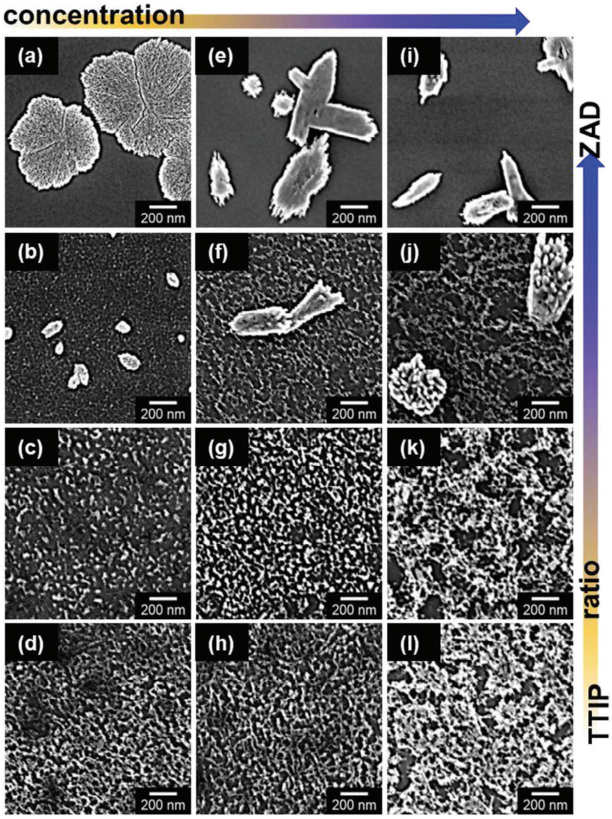

Figure 8. SEM images of zinc titanate and reference oxide thin films in series B after calcination. The ratios of the two precursors m_{TTIP}:m_{ZAD} are 10:0, 5:5, 3:7, and 0:10 (from the bottom to the top row). The material mass of the film (prepared using dilute, intermediate, and concentrated solutions) increases from the left to the right column.

(JCPDS 36–1451) is seen in its wurtzite phase, and for pure TTIP anatase TiO_2 (JCPDS 21–1272) is found. With the mixed precursors zinc titanate films formed. In case of a low HCl content (series A, Figure 10a), with increasing the ZAD contents (m_{TTIP}:m_{ZAD} = 5:5 and 3:7), $ZnTiO_3$ (JCPDS 39–0190) and $ZnTiO_x$(mixture) are formed, respectively. The detected signals for the A'$_{33}$ sample are indeed broad and weak, indicating that it is a mixture. The peak positions are close to those of $ZnTiO_3$ and Zn_2TiO_4, suggesting that the sample contains a mixture of these phases, which we abbreviate as “ZnTiOx”. In case of a high HCl content (series B, Figure 10b), with increasing the ZAD contents (m_{TTIP}:m_{ZAD} = 5:5 and 3:7), $ZnTiO_3$ and Zn_2TiO_4 (JCPDS 25–1164) are obtained, respectively. Thus, the precursor composition and HCl can be used to control the type of zinc titanate formed by the BCP-templated sol-gel chemistry approach presented here.

3. Conclusion

We synthesize thin hybrid and zinc titanate films using a PS-*b*-PEO templated sol-gel synthesis approach. For reference, also pure precursors ZAD and TTIP are used to synthesize ZnO and TiO_2 films. The HCl content (low and high), TTIP to ZAD ratios, and material mass (solution concentrations) affect the obtained film morphologies. These parameters also influence the morphology transitions of the calcined films.

At low HCl content (series A), the surface morphologies of the dilute solution-based films transform from disordered to ordered structures with an increasing ZAD content. Higher solution concentrations led to smaller domain sizes due to nanoscale structure compaction. In a high-concentration case, the impact of the ZAD content is diminished, likely due to polymer aggregation making BCP templating challenging.

Comparing the volume fractions of the internal and surface structures of the films, it turns out that the domain sizes of the internal structures are larger, which is attributed to the gradient installed by solvent evaporation and the competitive crystallization and microphase separation of the PEO blocks. At high HCl content (series B), an obvious increase in the domain sizes of the intermediate and concentrated solution films is seen with increasing ZAD content. We see a noticeable increase in the number of smaller domains because an increase in ions surrounding the polymer structure with increasing HCl content prevents aggregation, which is beneficial for BCP templating of the precursors to tailor the film morphology.

After calcination, we fabricate metal oxide films consisting of one-layer mesoporous films or two-layer films (top particle layer and bottom mesoporous structure layer). Small- and medium-sized domains remain stable before and after calcination, indicating a successful polymer template control. However, the large domains of the calcined films exceed template sizes due to the crystallite formation and structure collapse at high temperatures.

High HCl content decreases the hydrolysis rate of the precursor mixture, preventing large aggregate formation. Thus, the BCP template approach is successfully used to prepare stable and universal structures in zinc titanate thin films. Additionally, a broader range of parameters can be utilized to achieve template-controlled morphologies in the hybrid films. Crystallite formation and structural collapse during the calcination process are pathways to changing the initial template. While our study focuses on the influence of the relative composition of ZAD and TTIP on the film morphology, the effects of their absolute concentrations also merit investigation. Future studies could aim to explore how varying the specific concentrations of these precursors impacts the morphological characteristics of the resulting films. These issues can be mitigated by optimizing the calcination temperature and time. Our approach presents a promising one-step route for creating zinc titanate and other metal oxide films with controlled nanoscale mesoporous morphologies, offering substantial potential applications in sensors, supercapacitors, and biodevices.

4. Experimental Section

Materials: The amphiphilic diblock copolymer template, polystyrene-*block*-polyethylene oxide, (PS-*b*-PEO) was obtained from Polymer Source. Inc., Canada, and used as received. The number average molecular weight, M_n, for the PS and PEO blocks, were 20.5 and 8.0 kg mol^{-1} respectively, with a polydispersity index of 1.02. The titania precursor, namely titanium (IV) isopropoxide (TTIP; 97%), was a transparent liquid with a relative density of 0.96 g mL^{-1}; the zinc precursor was zinc acetate dehydrate (ZAD; 99.999% trace metal basis, a density of 1.84 g mL^{-1}). The above two precursors, N,N-dimethylformamide (DMF; analytical reagent grade

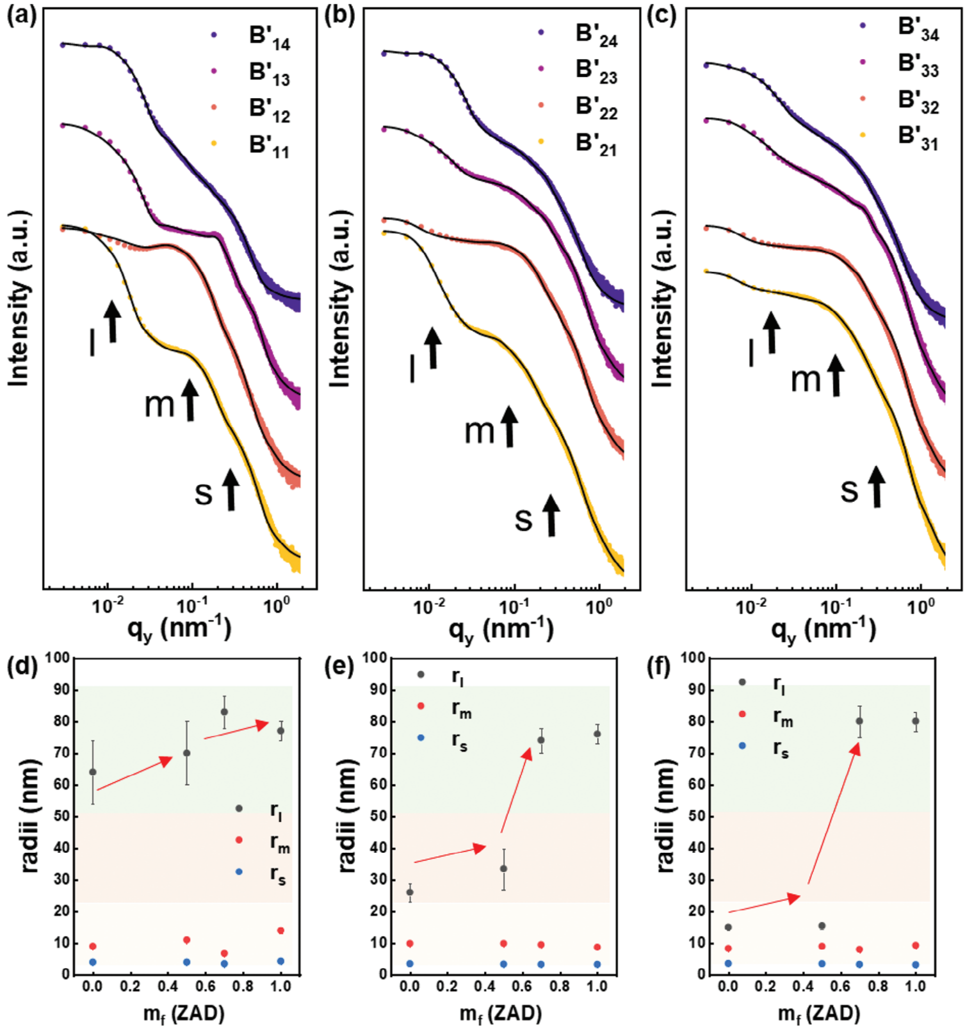

Figure 9. a–c) Horizontal line cuts from 2D GISAXS data of zinc titanate and reference oxide thin films in series B after calcination. The measured data are represented as solid circles and the modeling results are depicted as solid lines. To improve clarity, all curves have been shifted along the intensity axis. For the films using (a) dilute, (b) intermediate, and (c) concentrated solutions the ratios of m_{TTIP}:m_{ZAD} is 10:0, 5:5, 3:7, and 0:10 from bottom to top, respectively. Contributions from small (s), middle (m), and large (l) objects are indicated with the arrows. d–f) Extracted characteristic structure radii as a function of the mass ratio of ZAD in a precursor mixture, m_f (ZAD) for the (d) dilute, (e) intermediate and (f) concentrated solutions. With different colors the small (blue, r_s), middle (red, r_m), and large (black, r_l) objects are shown.

99.99%) and concentrated hydrochloric acid (HCl; 37%) were purchased from Sigma-Aldrich and used without further treatment.

Solution Preparation: In series A (low HCl content), the four solutions of c3 group were prepared with the following steps: Firstly PS-*b*-PEO (60 mg) was dissolved in DMF (200 uL) under continuous stirring for 0.5 h, then a mixture of HCl (88 uL) and DMF (800 uL) was slowly dropped in it under continuous stirring for 0.5 h, and then it was divided into two vials. After that, precursor solutions were prepared: 60 mg TTIP and 60 mg ZAD were dissolved into two 500 uL DMF vials to obtain the pure TTIP and ZAD solutions. Next, the precursor solutions were dropped into both polymer solutions to obtain the two stock solutions. Then, the two stock solutions were mixed with different mass fractions to obtain the final four solutions containing the four different precursor ratios (m_{TTIP}:m_{ZAD} = 10:0, 5:5, 3:7, 0:10) for the thin film preparation. These four samples from the concentrated solution system were diluted using 1 mL and 2 mL DMF to obtain the solution used for the intermediate and dilute solution systems, respectively. The prepared 12 samples were under continuous stirring overnight at room temperature for the next film preparation steps. In series B (high HCl content), the same solution-preparation process was used as series A, but a different amount of HCl of 176 uL was used. The solutions were transparent without precipitation, which was the general condition for the solution before the spin-coating step. The hybrid thin films composed of polymers and precursors were obtained by spin-coating (2000 rpm; 60 s) these different solutions on silicon substrates (2 × 2) cm^2 pre-cleaned in an acid bath.[34] To obtain the zinc titanate films and reference samples, the hybrid films were calcined at 600 °C in the air for 30 min in a tube furnace, RETTH 230/3, GERO *Hochtemperaturöfen* GmbH, with a heating rate of 5 °C min^{-1} from 25 to 600 °C.

Thin Film Characterization: The surface morphology of hybrid and zinc titanate thin films was characterized by high-resolution field emission SEM (Zeiss Gemini NVision 40) at a working distance of 5 mm and an acceleration voltage of 3 kV. GISAXS measurements were carried out on the P03 beamline of the PETRA III storage ring at DESY.[37] The following parameters were used: Wavelength was 1.048 Å, the sample-to-detector distance was 3901 mm, and X-ray photon energy was 11.83 keV. The scattering

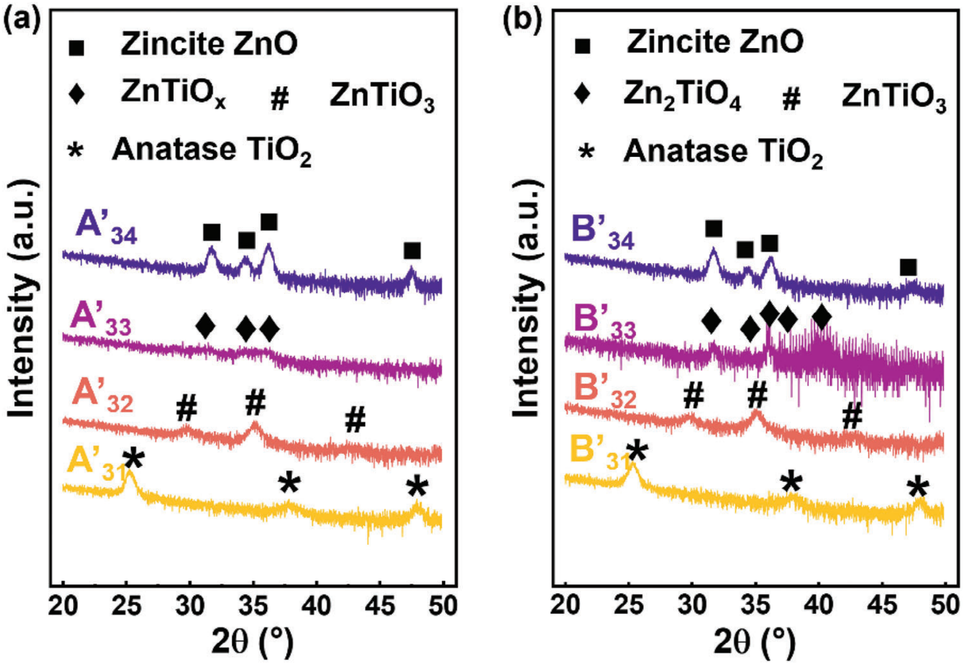

Figure 10. GIXD pattern of calcined films prepared with a) low and b) high HCl content for the different precursor ratios using the high concentration solutions. Characteristic peaks of the involved oxides and zinc titanate are labeled.

signal was detected using a Pilatus 300K detector (pixel size = 172 mm ×172 mm).[37] An incident angle of 0.4° was set to probe the inner structures of the thin film. A Python program named Directly Programmable Data Analysis Kit (DPDAK) was used for calibration and data analysis.[38] Horizontal line cuts of the 2D GISAXS data were performed at the Yoneda peak position. Details of the beamline were reported elsewhere.[39]

Grazing-incidence X-ray diffraction (GIXD) was performed with a D8 ADVANCE X-ray diffractometer using an X-ray wavelength of 1.54 Å at 2θ(Cu-Kα) = 20–50°. GIXD measurements were performed with X'Pert PRO PANalytical instrument (Bragg–Brentano geometry with fixed divergence slits, continuous mode, position sensitive detector, Cu-Kα radiation, Ni filter).

For the thermogravimetric analysis (TGA), a Mettler Toledo TGA 2 instrument was used to record the sample's mass versus time for two predefined temperature profiles. The first profile consisted of three main steps: The heating step from 25 °C to 600 °C; the isothermal step at a fixed temperature of 600 °C for 30 min, and the cooling step from 800 °C to 25 °C. For the heating/cooling steps, a rate of 5 °C min^{-1} was used. The O_2 gas flow was set to 20 mL min^{-1} for all steps.

Supporting Information

Supporting Information is available from the Wiley Online Library or from the author.

Acknowledgements

The authors thank Deutsche Forschungsgemeinschaft (DFG) for financial support via the International Research Training Group 2022 the Alberta/Technical University of Munich International Graduate School for Environmentally Responsible Functional Materials (ATUMS), project MU1487/32, IRTG2022 and under Germany's Excellence Strategy – EXC 2089/1–390776260 (e-conversion) as well as from TUM.solar in the context of the Bavarian Collaborative Research Project Solar Technologies Go Hybrid (SolTech). Y.L. and S.Y. acknowledge the financial support from the China Scholarship Council (CSC). W.C. acknowledges the funding support from the National Natural Science Foundation of China (No. 12204318), Guangdong Basic and Applied Basic Research Foundation (No. 2021A1515110535), and Shenzhen Science and Technology Program (Grant No. RCYX20221008092908030, ZDSYS20200811143600001). The authors thank Prof. Alexander Holleitner and Peter Weiser for providing access to the SEM, Guangjiu Pan for help with the GIXD measurements, and Matthias Schwartzkopf and Andrei Chumakov for technical support at P03. All GISAXS measurements were carried out at the light source PETRA III at DESY, a member of the Helmholtz Association (HGF).

Open access funding enabled and organized by Projekt DEAL.

Conflict of Interest

The authors declare no conflict of interest.

Data Availability Statement

The data that support the findings of this study are available from the corresponding author upon reasonable request.

Keywords

calcination process, film morphology evolution, mesoporous structure, sol-gel chemistry, zinc titanate

Received: March 10, 2024
Revised: June 27, 2024
Published online: September 4, 2024

---

[1] a) E. J. Crossland, N. Noel, V. Sivaram, T. Leijtens, J. A. Alexander-Webber, H. J. Snaith, *Nature* **2013**, *495*, 215; b) S. Valastro, E. Smecca,

G. Mannino, C. Bongiorno, G. Fisicaro, S. Goedecker, V. Arena, C. Spampinato, I. Deretzis, S. Dattilo, *Nat. Sustain.* **2023**, 6, 974; c) N. Asim, M. Mohammad, M. Badiei, in *Nanomaterials for green energy*, Elsevier, Amsterdam, The Netherlands **2018**, p., 227; d) I. Mironyuk, L. Soltys, T. Tatarchuk, V. Tsinurchyn, *Phys. Chem. Solid State* **2020**, *21*, 300; e) S. Liang, X. Wang, Y.-J. Cheng, Y. Xia, P. Mueller-Buschbaum, *Energy Storage Mater.* **2022**, *45*, 201; f) D. Liu, T. L. Kelly, *Nat. Photonics* **2014**, *8*, 133; g) A. Polman, M. Knight, E. C. Garnett, B. Ehrler, W. C. Sinke, *Science* **2016**, *352*, aad4424.

[2] a) X. Sun, C. Wang, D. Su, G. Wang, Y. Zhong, *Adv. Mater. Technol.* **2020**, *5*, 1900993; b) N. Fumeaux, D. Briand, *npj Flexible Electron.* **2023**, *7*, 14.

[3] a) R. Ameta, M. S. Solanki, S. Benjamin, S. C. Ameta, in *Advanced oxidation processes for waste water treatment*, Elsevier, Amsterdam, The Netherlands **2018**, p. 135; b) M. Azizi-Lalabadi, A. Ehsani, B. Divband, M. Alizadeh-Sani, *Sci. Rep.* **2019**, *9*, 17439; c) J. Ma, C. Zhu, K. Mao, W. Jiang, J. Low, D. Duan, H. Ju, D. Liu, K. Wang, Y. Zang, *Nat. Commun.* **2023**, *14*, 1410; d) Q. Zheng, J. Williams, L. R. van Thiel, S. V. Elgersma, M. D. Mantle, A. J. Sederman, T. A. Baart, G. L. Bezemer, C. M. Guédon, L. F. Gladden, *Nat. Catal.* **2023**, *6*, 185.

[4] a) J. Chen, F. Qiu, W. Xu, S. Cao, H. Zhu, *Appl. Catal., A* **2015**, *495*, 131; b) A. A. Ismail, D. W. Bahnemann, *J. Mater. Chem.* **2011**, *21*, 11686; c) S. Chirumbolo, D. Gibellini, L. Berto, C. Cirrito, A. Vella, G. Bjørklund, A. Sbarbati, P. Bernardi, U. Tirelli, *Sci. Rep.* **2023**, *13*, 4200; d) H. C. Fry, Y. Liu, N. M. Dimitrijevic, T. Rajh, *Nat. Commun.* **2014**, *5*, 4606; e) H. Tang, Y. Su, B. Zhang, A. F. Lee, M. A. Isaacs, K. Wilson, L. Li, Y. Ren, J. Huang, M. Haruta, *Sci. Adv.* **2017**, *3*, 1700231; f) S. H. Ko, D. Lee, H. W. Kang, K. H. Nam, J. Y. Yeo, S. J. Hong, C. P. Grigoropoulos, H. J. Sung, *Nano Lett.* **2011**, *11*, 666.

[5] a) F. Guo, X. Sun, B. Liu, Z. Yang, J. Wei, D. Xu, *Angew. Chem.* **2019**, *131*, 18631; b) H. Wu, Y. Min, Q. Zhang, W. Li, J. Yuan, Z. Wu, S. Wang, *RSC Adv.* **2016**, *6*, 103822; c) N. Pal, M. Paul, A. Bhaumik, *Appl. Catal., A* **2011**, *393*, 153.

[6] J. Li, B. Wu, Q. Zhang, H. Wang, Y. Li, *J. Nanosci. Nanotechnol.* **2016**, *16*, 9568.

[7] a) S. F. Bartram, R. A. Slepetys, *J. Am. Ceram. Soc.* **1961**, *44*, 493; b) M. Mohammadi, D. Fray, *J. Eur. Ceram. Soc.* **2010**, *30*, 947; c) M. Zhao, B. P. Bastakoti, Y. Li, H. Xu, J. Ye, Z. Liu, Y. Yamauchi, *Chem. Commun.* **2015**, *51*, 14582.

[8] C. Chuaicham, S. Karthikeyan, J. T. Song, T. Ishihara, B. Ohtani, K. Sasaki, *ACS Appl. Mater. Interfaces* **2020**, *12*, 9169.

[9] a) J. Yu, D. Li, L. Zhu, X. Xu, *J. Alloys Compd.* **2016**, *681*, 88; b) L. Pan, G.-Q. Shen, J.-W. Zhang, X.-C. Wei, L. Wang, J.-J. Zou, X. Zhang, *Ind. Eng. Chem. Res.* **2015**, *54*, 7226.

[10] a) Q. Zhang, C. S. Dandeneau, X. Zhou, G. Cao, *Adv. Mater.* **2009**, *21*, 4087; b) J. Lin, Y.-U. Heo, A. Nattestad, Z. Sun, L. Wang, J. H. Kim, S. X. Dou, *Sci. Rep.* **2014**, *4*, 5769.

[11] K. Nakata, A. Fujishima, *J. Photochem. Photobiol., C* **2012**, *13*, 169.

[12] Y. Chi, Q. Yuan, S. Hou, Z. Zhao, *Ceram. Int.* **2016**, *42*, 5094.

[13] X. Yu, V. De Waele, A. Löfberg, V. Ordomsky, A. Y. Khodakov, *Nat. Commun.* **2019**, *10*, 700.

[14] a) B. Fotovvati, N. Namdari, A. Dehghanghadikolaei, *J. Manuf. Mater. Process.* **2019**, *3*, 28; b) R. Sui, P. Charpentier, *Chem. Rev.* **2012**, *112*, 3057.

[15] Y. Xu, K. C. Tijssen, P. H. Bomans, A. Akiva, H. Friedrich, A. P. Kentgens, N. A. Sommerdijk, *Nat. Commun.* **2018**, *9*, 2582.

[16] a) S. H. Kim, M. J. Misner, T. Xu, M. Kimura, T. P. Russell, *Adv. Mater.* **2004**, *16*, 226; b) K. Yu, A. Eisenberg, *Macromolecules* **1998**, *31*, 3509.

[17] L. Zhang, K. Yu, A. Eisenberg, *Science* **1996**, *272*, 1777.

[18] a) Z. Tang, D. Li, J. Lin, L. Zhang, C. Cai, Y. Yao, C. Yang, X. Tian, *Polym. Chem.* **2020**, *11*, 7487; b) J. A. Ramos, L. H. Espósito, R. Fernández, I. a. Zalakain, S. Goyanes, A. Avgeropoulos, N. E. Zafeiropoulos, G. Kortaberria, I. a. Mondragon, *Macromolecules* **2012**, *45*, 1483.

[19] R. H. Rice, P. Mokarian-Tabari, W. P. King, R. Szoszkiewicz, *Langmuir* **2012**, *28*, 13503.

[20] a) E. Han, K. O. Stuen, Y.-H. La, P. F. Nealey, P. Gopalan, *Macromolecules* **2008**, *41*, 9090; b) Y. Mai, A. Eisenberg, *Chem. Soc. Rev.* **2012**, *41*, 5969.

[21] a) S. H. Kim, M. J. Misner, L. Yang, O. Gang, B. M. Ocko, T. P. Russell, *Macromolecules* **2006**, *39*, 8473; b) S. C. Park, B. J. Kim, C. J. Hawker, E. J. Kramer, J. Bang, J. S. Ha, *Macromolecules* **2007**, *40*, 8119.

[22] a) T. Kimura, M. Shintate, N. Miyamoto, *Chem. Commun.* **2015**, *51*, 1230; b) W. van Zoelen, G. Ten Brinke, *Soft Matter* **2009**, *5*, 1568; c) B. P. Bastakoti, S. Ishihara, S.-Y. Leo, K. Ariga, K. C.-W. Wu, Y. Yamauchi, *Langmuir* **2014**, *30*, 651.

[23] a) N. Li, L. Song, L. Bießmann, S. Xia, W. Ohm, C. J. Brett, E. Hadjixenophontos, G. Schmitz, S. V. Roth, P. Müller-Buschbaum, *Adv. Mater. Interfaces* **2019**, *6*, 1900558; b) S. Yin, L. Song, S. Xia, Y. Cheng, N. Hohn, W. Chen, K. Wang, W. Cao, S. Hou, P. Müller-Buschbaum, *Small Methods* **2020**, *4*, 1900689.

[24] a) K. Wang, V. Körstgens, D. Yang, N. Hohn, S. V. Roth, P. Müller-Buschbaum, *J. Mater. Chem. A* **2018**, *6*, 4405; b) A. Carretero-Genevrier, G. L. Drisko, D. Grosso, C. Boissiere, C. Sanchez, *Nanoscale* **2014**, *6*, 14025.

[25] J. Qiu, W. Yu, X. Gao, X. Li, W. He, S.-J. Park, H.-K. Kim, Y.-H. Hwang, *J. Sol-Gel Sci. Technol.* **2008**, *47*, 187.

[26] X. Jiang, N. Suzuki, B. P. Bastakoti, W. J. Chen, Y. T. Huang, Y. Yamauchi, *Eur. J. Inorg. Chem.* **2013**, *2013*, 3286.

[27] T. Tian, S. Tu, A. Xu, S. Yin, A. L. Oechsle, T. Xiao, A. Vagias, J. Eichhorn, J. Suo, Z. Yang, *Adv. Funct. Mater.* **2024**, *34*, 2311793.

[28] K. Sarkar, E. V. Braden, T. Fröschl, N. Hüsing, P. Müller-Buschbaum, *J. Mater. Chem. A* **2014**, *2*, 15008.

[29] M. A. Ehsan, H. Khaledi, A. Pandikumar, P. Rameshkumar, N. M. Huang, Z. Arifin, M. Mazhar, *New J. Chem.* **2015**, *39*, 7442.

[30] a) S. Mustapha, M. Ndamitso, A. Abdulkareem, J. Tijani, D. Shuaib, A. Ajala, A. Mohammed, *Appl. Water Science* **2020**, *10*, 49; b) G. Iannaccone, A. Bernardi, R. Suriano, C. L. Bianchi, M. Levi, S. Turri, G. Griffini, *RSC Adv.* **2016**, *6*, 46915.

[31] a) W. Guo, C. Xu, X. Wang, S. Wang, C. Pan, C. Lin, Z. L. Wang, *J. Am. Chem. Soc.* **2012**, *134*, 4437; b) S. J. Kim, S. D. Park, Y. H. Jeong, S. Park, *J. Am. Ceram. Soc.* **1999**, *82*, 927; c) E. Hosono, S. Fujihara, K. Kakiuchi, H. Imai, *J. Am. Chem. Soc.* **2004**, *126*, 7790.

[32] a) K. Brassat, J. K. Lindner, *Adv. Mater. Interfaces* **2020**, *7*, 1901565; b) T. Rejek, P. Schweizer, D. Joch, L. Portilla, E. Spiecker, M. Halik, *Macromolecules* **2020**, *53*, 5604.

[33] T. Tian, S. Yin, S. Tu, C. L. Weindl, K. S. Wienhold, S. Liang, M. Schwartzkopf, S. V. Roth, P. Müller-Buschbaum, *Adv. Funct. Mater.* **2021**, *31*, 2105644.

[34] P. Müller-Buschbaum, *Eur. Phys. J. E* **2003**, *12*, 443.

[35] C. J. Brett, N. Mittal, W. Ohm, M. Gensch, L. P. Kreuzer, V. Körstgens, M. Månsson, H. Frielinghaus, P. Müller-Buschbaum, L. D. Söderberg, *Macromolecules* **2019**, *52*, 4721.

[36] A. L. Oechsle, J. E. Heger, N. Li, S. Yin, S. Bernstorff, P. Müller-Buschbaum, *ACS Appl. Mater. Interfaces* **2022**, *14*, 30802.

[37] A. Buffet, A. Rothkirch, R. Döhrmann, V. Körstgens, M. M. Abul Kashem, J. Perlich, G. Herzog, M. Schwartzkopf, R. Gehrke, P. Müller-Buschbaum, *J. Synchrotr. Radiat.* **2012**, *19*, 647.

[38] G. Benecke, W. Wagermaier, C. Li, M. Schwartzkopf, G. Flucke, R. Hoerth, I. Zizak, M. Burghammer, E. Metwalli, P. Müller-Buschbaum, *J. Appl. Crystallogr.* **2014**, *47*, 1797.

[39] G. Santoro, A. Buffet, R. Döhrmann, S. Yu, V. Körstgens, P. Müller-Buschbaum, U. Gedde, M. Hedenqvist, S. Roth, *Rev. Sci. Instrum.* **2014**, *85*, 043901.